Concurrent superimposed ice formation and meltwater runoff on Greenland's ice slabs

Tedstone, Andrew; Machguth, Horst; Clerx, Nicole; Jullien, Nicolas; Picton, Hannah; Ducrey, Julien; van As, Dirk; Colosio, Paolo; Tedesco, Marco; Lhermitte, Stef

DOI
10.1038/s41467-025-59237-9

Publication date
2025

Document Version
Final published version

Published in
Nature Communications

Citation (APA)
Tedstone, A., Machguth, H., Clerx, N., Jullien, N., Picton, H., Ducrey, J., van As, D., Colosio, P., Tedesco, M., & Lhermitte, S. (2025). Concurrent superimposed ice formation and meltwater runoff on Greenland's ice slabs. *Nature Communications*, *16*(1), Article 4494. https://doi.org/10.1038/s41467-025-59237-9

nature communications

Article

https://doi.org/10.1038/s41467-025-59237-9

Concurrent superimposed ice formation and meltwater runoff on Greenland's ice slabs

Received: 7 June 2024

Accepted: 14 April 2025

Andrew Tedstone[1,2] ✉, Horst Machguth[1], Nicole Clerx[1,9], Nicolas Jullien[1], Hannah Picton[3], Julien Ducrey[1], Dirk van As[4], Paolo Colosio[5], Marco Tedesco[6] & Stef Lhermitte[7,8]

Rivers and slush fields on the Greenland Ice Sheet increasingly develop in locations where the accumulation zone hosts near-impermeable ice slabs. However, the division between runoff versus retention in these areas remains unmeasured. We present field measurements of superimposed ice formation onto slabs around the visible runoff limit. The quantity of superimposed ice varies by proximity to visible surface water and the surface slope, highlighting that meltwater can flow laterally before refreezing. We use heat conduction modelling and radar observations of autumn wetness to show that in our field area in 2022, 65% of superimposed ice formed during summer and the rest during autumn in the relict supraglacial hydrological network. Overall, 84% of melt around the visible runoff limit refroze. Ice-sheet-wide we estimate that slabs refroze 56 gigatonnes of melt (26-69 gigatonnes according to slab extent) between 2017 and 2022. Slabs are thus both hotspots of refreezing and emerging zones of runoff.

In the accumulation area of the Greenland Ice Sheet where the surface is underlain by firn, meltwater generally percolates into the firn pore space where it refreezes in-situ, and therefore does not run off. Surface mass balance (SMB) modelling indicates that in the past several decades 40-50% of ice-sheet-wide melt has refrozen in the firn[1–3]. This makes firn an important buffer against future sea level rise[4,5]. However, in the last three decades surface melting has increased more quickly than accumulation[6]. In the lower accumulation area the firn pore space has decreased anomalously as a result of intense meltwater percolation and refreezing[4,7], leading to metres-thick near-impermeable ice 'slabs' forming just below the ice sheet surface[8,9]. Meanwhile, the visible runoff area—the area drained by surface river networks—has expanded by 29% in the past four decades, with concomitant increases in the elevation of the visible runoff limit[10]. This expansion has mainly occurred along the ice sheet's western and northern flanks in areas now underlain by ice slabs[11]. According to synthetic aperture radar observations, ice slabs are estimated to underlie ~150,000 km^2 of the ice sheet, though they may occupy as little as ~60,000 km^2 or as much as ~220,000 km^2 (ref. 12).

In-situ hydrological observations around the runoff limit on top of an ice slab show that surface meltwater percolates through the overlying snowpack and firn then flows laterally through a slush matrix on top of the ice slab before it reaches a surface stream or river. This matrix is up to several decimetres thick and supports flow speeds ranging from 1.3 to 15.1 m h^{-1} (ref. 13)—roughly three orders of magnitude slower than subsequent open river flow of 1–3 m s^{-1} (ref. 14). A slush matrix on top of a cold ice slab is therefore a potential source for superimposed ice formation onto the slab surface as its wet pore space gets refrozen from the bottom up[15].

On the Greenland Ice Sheet, studies of refreezing have generally focused on vertical infiltration and refreezing in porous firn above the runoff limit[7,16,17], sometimes considering decimetre-scale horizontal flow fingers[18]. Field measurements north of Jakobshavn Isbrae during the 2000s were suggestive of slow water migration at depth beneath multiple ice layers but in the absence of ice slabs, indicative of a gradient between complete refreezing and complete runoff[5,19]. Measurements of superimposed ice formation specifically have predominantly

---

[1]Department of Geosciences, University of Fribourg, Fribourg, Switzerland. [2]Institute of Earth Surface Dynamics, University of Lausanne, Lausanne, Switzerland. [3]School of Geosciences, University of Edinburgh, Edinburgh, UK. [4]Geological Survey of Denmark and Greenland, Copenhagen, Denmark. [5]DICATAM, University of Brescia, Brescia, Italy. [6]Lamont-Doherty Earth Observatory, Columbia University, New York, USA. [7]Department of Earth and Environmental Sciences, KU Leuven, Leuven, Belgium. [8]Department of Geoscience and Remote Sensing, Delft University of Technology, Delft, Netherlands. [9]Present address: École Polytechnique Fédérale de Lausanne, Lausanne, Switzerland. ✉e-mail: andrew.tedstone@unil.ch

been made elsewhere such as Svalbard[20,21] or the Canadian Arctic e.g. [22,23]. Thickening of Greenland's ice slabs during years in which they supported surface river development can be observed in repeat airborne radar measurements[11], yet the contribution of refreezing in ice slab areas to SMB has not been quantified.

Here we present measurements of superimposed ice formation (hereafter SIF) on top of ice slabs on the K-Transect (67 ° N), south-west Greenland, acquired during two years in which the visible runoff limit intersected the area. We estimate the impact of SIF on net water discharge from the hydrological catchment and on SMB. Then, in conjunction with vertical heat flow modelling and synthetic aperture radar observations of sub-surface wetness, we make an assessment of the importance of SIF to SMB across all regions of the ice sheet underlain by ice slabs.

Results

Superimposed ice formation depends on near-surface water flow

We measured SIF in the 2021 and 2022 melt seasons through repeat in-situ observations at stakes located 1760–1825 m above sea level (a.s.l.) (Fig. 1a-c; Methods; Suppl. Fig. 1), more than 200 m higher than the long-term equilibrium line altitude of ~1550 m a.s.l[24]. The average surface slope is ~0. 3°[13]. Across the elevation range spanned by our study area, melt derived from a surface energy balance model forced by in-situ observations[25] was relatively uniform, with 0.33–0.46 m w.e. in 2021 and 0.26–0.33 m w.e. in 2022 (Methods). In 2017 the area was underlain by an ice slab with an average thickness and standard deviation of 8.7 ± 3.9 m[11]. The area developed surface slush fields and rivers or linear drainage pathways suggestive of runoff every summer between 2011 and 2023 except 2017 and 2018[10].

Between April/May 2021 and 2022 (hereafter '2021') we measured SIF at three sites (FS1–3), and between April/May 2022 and 2023 (hereafter '2022') we made measurements at eleven sites along two transects. One transect was perpendicular to the main visible drainage pathway through the area (and co-located with the line of summer hydrological measurements by ref. 13) while the second transect was normal to the first and ran west-east, parallel to the general surface slope.

SIF was spatially heterogeneous and corresponded with the locations of surface water presence near to the peak of the melt season and the surface slope, as follows (Fig. 1d). (i) Considering the largest measurements of SIF (BH0, BH1, FS2 in 2021), all were located within tens of metres of a major river or linear drainage pathway and on very shallow slopes. (ii) The other sites with relatively high SIF (FS1, BH5, 3u3) were further away from linear drainage pathways and

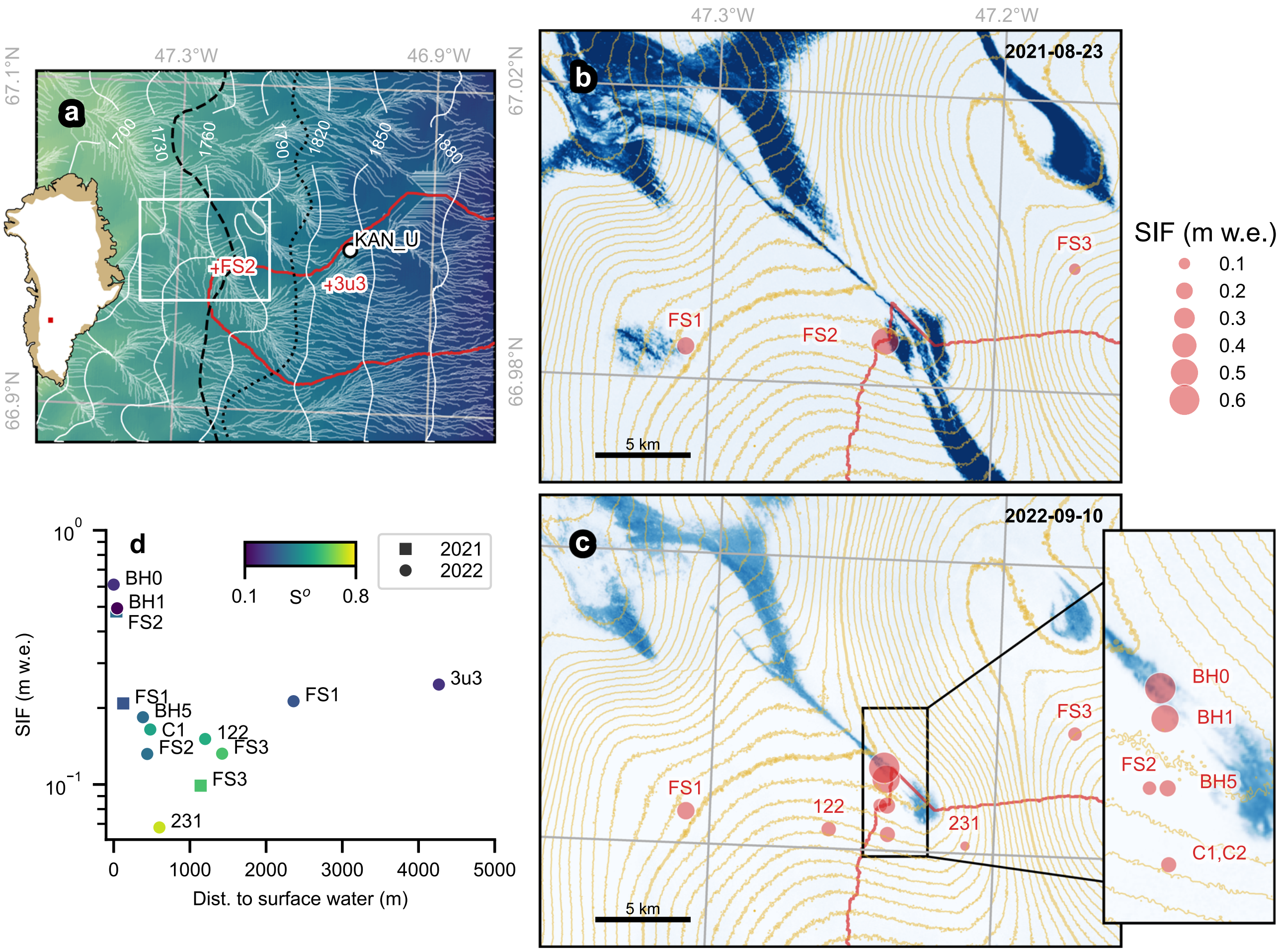

Fig. 1 | In-situ measurements of superimposed ice formation (SIF) in south-west Greenland. a ArcticDEM[42] with contours (m a.s.l.) every 30 m. White lines show the expected surface river network according to hydrological terrain analysis (Methods). Measurement sites FS2 and 3u3 are shown by crosses. The automatic weather station KAN_U, used for surface energy balance modelling, is shown by the white circle. Red line delineates the surface hydrological catchment of FS2. Black lines show maximum visible runoff limits according to Copernicus Sentinel-2 imagery in 2021 (dotted) and 2022 (dashed). White box shows location of panels **b** and **c**. **b–c** In-situ measurements of SIF are indicated by red circles, size proportional to quantity (m w.e.), overlaid on Copernicus Sentinel-2 NDWI_{ICE} showing the maximum surface hydrology extent in that particular year (Methods). Contours every 2 m; the 1760 and 1790 m a.s.l. contours (panel a) in bold. **b** Scene acquired on 23 August 2021. **c** Scene acquired on 10 September 2022, with enlarged panel of north-south transect. **d** For each SIF measurement site, the Euclidean distance to the nearest surface water, including slush fields, versus the measured SIF. Colour indicates slope angle (S°; degrees). Source data are provided in Source Data files.

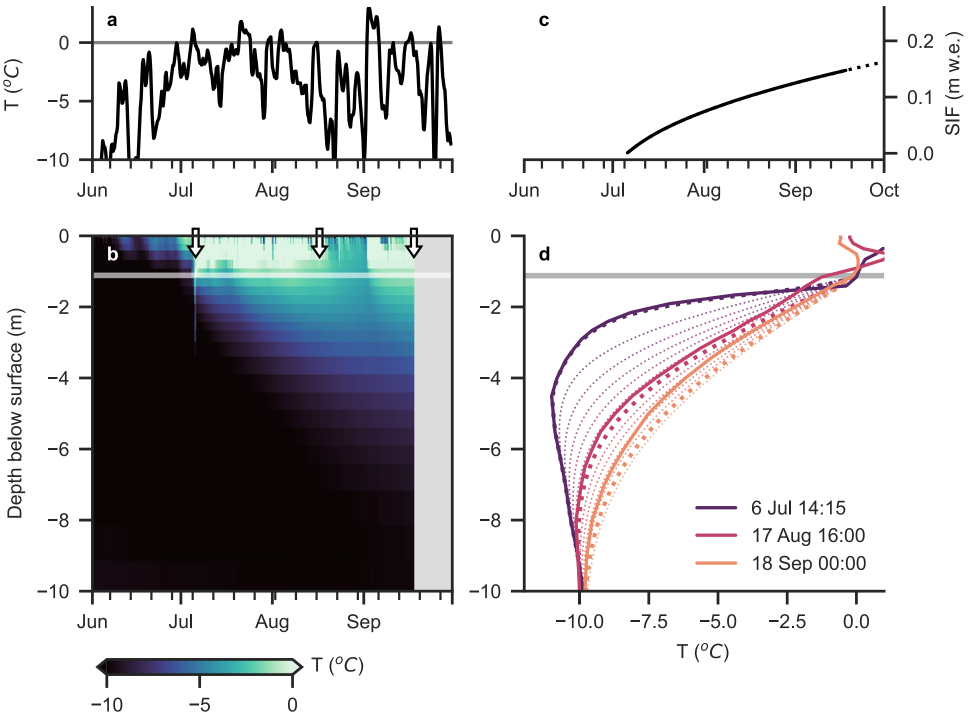

Fig. 2 | Ice slab warming and superimposed ice formation (SIF) at FS2. **a** Measurements of air temperature (T) and **b** sub-surface temperatures. Upper surface of the ice slab in May 2022 shown by white line. Arrows correspond to measured temperature profiles shown in panel d. Temperature (T) measurements are spaced every 0.15 m in the vicinity of the upper slab surface and are shown until recording stopped (Methods). **c** Modelled cumulative SIF during the 2022 melt season from 6 Jul to 18 Sep (solid line) and continuing beyond the end of the melt season (dashed line). **d** Calculated slab temperature profiles (T, dotted lines) every 7 d starting on 6 Jul (purple) and ending on 28 Sep (red). Measured temperature profiles (solid lines) are plotted for comparison with temporally-closest calculated profile (thick dotted lines). Upper surface of the ice slab in May 2022, i.e. before accretion during the 2022 melt season, is shown by grey line. Source data are provided in Source Data files.

did not necessarily have surface water nearby. At FS1 there was 0.21 and 0.21 m w.e. SIF in 2021 and 2022 respectively, even though a slush field was only visible nearby in 2021. Similarly, site 3u3 also recorded substantial SIF in 2022 despite being 4 km away from visible surface water, but Sentinel-2 imagery from recent high-melt years (e.g. 2019, 2023) shows that 3u3 lies within a few hundred metres of the axis of the same linear drainage pathway which flows past FS2. We therefore interpret the larger SIF at these sites as indicative of a higher local water table as the near-zero slope is conducive to ponding of water supplied by sub-surface flow inside the snowpack from the surrounding area[13]. (iii) Considering the remaining measurements with less SIF (C1/C2, 122, FS3, 231, FS2 in 2022), all were located at least hundreds of metres away from visible surface water, i.e. more distal to the main drainage axis of the catchment, and all (apart from FS2) had steeper slopes compared to the other measurement sites. The role of a steeper slope in reducing SIF is particularly evident at site 231.

Considering only measurements from 2022 and excluding those sites proximal to a linear drainage pathway (BH0 and BH1), average SIF was 0.16 ± 0.05 m w.e. (± 1 standard deviation; $n = 9$). These sites had an average climatological surface mass balance (cSMB) calculated from repeat firn cores (Methods) of 0.53 ± 0.06 m w.e., of which SIF constituted 30 ± 9 %. In comparison, BH0 and BH1 had a larger cSMB of 0.77 ± 0.09 m w.e. yr^{-1} ($n = 2$), of which SIF constituted 72 ± 3 %. As melt is near-uniform across the area of our observations, these measurements reinforce that meltwater for SIF is supplied not only by local melt production but also by lateral water flow.

Ice slab cold content determines summertime SIF

We now focus on the mechanisms of SIF onto the ice slab's uppermost surface. We installed a 12 m thermistor string in a borehole at FS2 in May 2022, suspended from a mast frozen into the sub-surface (Methods). It recorded the warming of the overlying snowpack during the early melt season, becoming isothermal on 6 July which enabled meltwater delivery to the ice slab surface (Fig. 2a, b). We then observed subsequent ice slab warming to at least 6 m depth, indicating refreezing of the surface water on to the top of the slab surface which warmed the slab below as latent heat is released. We term this mode of SIF 'bottom-up' as the cold content comes from the underlying slab (Fig. 3, Summer).

To calculate how much SIF can occur during summer, we modelled SIF potential as a 0 °C slush matrix refreezing onto a cold impermeable ice slab due to heat conduction, a purely thermal approach that assumes infinite and instantaneous melt availability (Methods). We initialised our model with the vertical temperature profile measured on 6 July, the first day that the ice slab surface reached 0 °C. We modelled SIF and the slab temperature profile for the duration of the melt season, assuming a constant 0°C at the slab surface.

Our calculations yield 0.15 m w.e. summer bottom-up SIF by the end of the 2022 melt season on 18 Sep (Fig. 2c), agreeing well with our measured total 0.16 ± 0.05 m w.e. yr^{-1} SIF away from surface hydrological features. Calculated temperature profiles show overall good agreement with measurements (Fig. 2d), with a slight warm bias: at the end of the melt season on 18 September, the modelled temperature profile was on average 0. 4°C warmer than observed. The observed 18 September profile was reproduced most closely by the model on 3 September, which suggests that the model overestimated SIF by 0.02 m w.e., perhaps due to continuing to simulate SIF during the melt hiatus in late August 2022. Nonetheless, overall our model reproduces the observed seasonal slab warming driven by latent heat release during SIF. These results are evidence that away

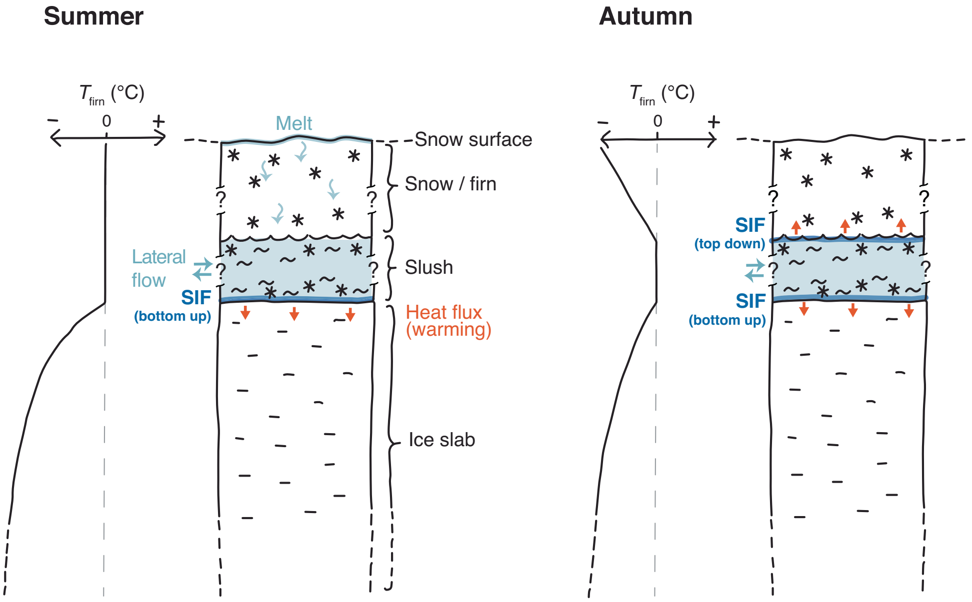

Fig. 3 | Sketch of superimposed ice formation (SIF) drivers during summer and autumn. Summer: A wet slush matrix is perched on top of an impermeable ice slab several metres thick and is overlain by an isothermal snowpack. SIF proceeds `bottom-up' on the surface of the slab; the release of latent heat as water freezes causes the slab to progressively warm (T_{firn}). Autumn: The slab has warmed compared to the start of summer. At locations where meltwater has collected but not yet refrozen, the slush matrix remains wet and likely now overlain by a cold snowpack. `Bottom-up' SIF continues, together with `top-down' SIF as freezing surface temperatures penetrate the top of the slush matrix. In both panels, question marks indicate unconstrained snowpack and slush matrix thicknesses.

from surface hydrological features, 94 % of SIF (at 0.16 m w.e. yr^{-1}; 68-100% considering the standard deviation of our observations of ± 0.05 m w.e. yr^{-1}) can be explained by direct refreezing of local surface melt during summer once it has percolated through the overlying snow/slush matrix.

Localised SIF continues into autumn

While summertime SIF was generally sufficient to accommodate local meltwater generation and percolation in 2022, our in-situ measurements also indicate that much larger quantities of SI formed in specific areas. We argue that these larger amounts of SI can be explained by lateral melt transport through the slush matrix (as observed by ref. 13) and localised ponding which provides residual meltwater supply for SIF to continue in specific locations in autumn, beyond the end of the melt season.

To map the duration of residual wetness in the uppermost decimetres to metres of the firn column after the melt season, we used satellite C-band Synthetic Aperture Radar (SAR) measurements of Horizontal-Vertical polarisation backscatter intensity, de-biased relative to wintertime and then thresholded at -2.17 dB (Methods). This approach is similar to previous studies which have used Sentinel-1 to detect firn aquifers in Greenland[26] and snow melt in Antarctica[27]. Five days after the end of melting, 60 % of the study area remained wet; 30 % was still wet after 18 days (Fig. 4a,b). By 66 days after melting, 99 % of the area was refrozen.

In autumn freezing air temperatures predominate (Fig. 4c). These cool the snowpack from above, so 'top-down' SIF presumably occurs in parallel with bottom-up SIF as slab cold content continues to be consumed (Fig. 3). We modelled these two modes as follows: we calculated bottom-up SIF by continuing our summer model run into autumn, until residual wetness disappeared. Separately, we estimated top-down SIF by heat conduction away from the slush through the snowpack to the cold atmosphere (Methods). Based on our thermistor string measurements (Fig. 2), the snowpack thickness above the slush was approximately 0.6 m at the start of autumn. As this is the most sensitive parameter in our model, we assessed top-down SIF in our study area occurring beneath snowpacks of 0.6 m, 0.3 m (0.5×) and 0.9 m (1.5×) thickness. We then used our retrievals of residual wetness duration to identify the SIF contribution from each of the two autumn SIF modes.

Autumn bottom-up SIF proceeds at a slower rate than in summer, reflecting the diminished ice slab cold content and with little sensitivity to the ± 1°C uncertainty in the initial temperature at 10 m depth[28] (Fig. 4c). Meanwhile, the start of top-down SIF is delayed by the requirement to first refreeze irreducible water content in the overlying snowpack. It then commences at a similar rate to bottom-up SIF, subsequently diverging as a function of snowpack thickness, especially in the case of a thin snowpack which cools very quickly in comparison to a thicker pack. Whether a slush matrix that is thick enough to produce ~0.4 m w.e. top-down SIF over 60 d can co-exist with a sufficiently thin snowpack is unclear as we lack constraints from the field, but observations made in the area during summer 2020[13] suggest that such conditions are unlikely.

Total SIF at the visible runoff limit

We summed our pixel-by-pixel estimates of summer and autumn SIF introduced above to derive total SIF over our field study area (Fig. 5a, b). Considering melt of 0.26–0.33 m between 1700 and 1800 m a.s.l., areas with surface hydrological features (e.g. around BH0) refroze substantially more meltwater than they produced. Our model-derived values of total SIF compare reasonably well with our in-situ measurements (Fig. 5c, R^2 0.66, p <0.01, n = 10). We note that the lack of modelled variability around 0.2 m w.e. is likely to be associated with the 12-day resolution of the Sentinel-1 observations. Considering the outlier of site 231, calculated SIF was roughly 0.3 m w.e. too high due to prolonged autumn wetness. This site was located in the margins of the wet subsurface area (Fig. 5b) but was not visibly wet and had a locally steeper slope (Fig. 1c, d); the wetness conditions observed by SAR over tens of metres therefore likely obscured the most local patterns of wetness.

We examined summed total SIF in the first 10 km of FS2's upstream hydrological catchment, roughly corresponding to the plausible limit of sub-surface hydrological routing based on SAR residual wetness (Fig. 4a). In addition to our best-estimate

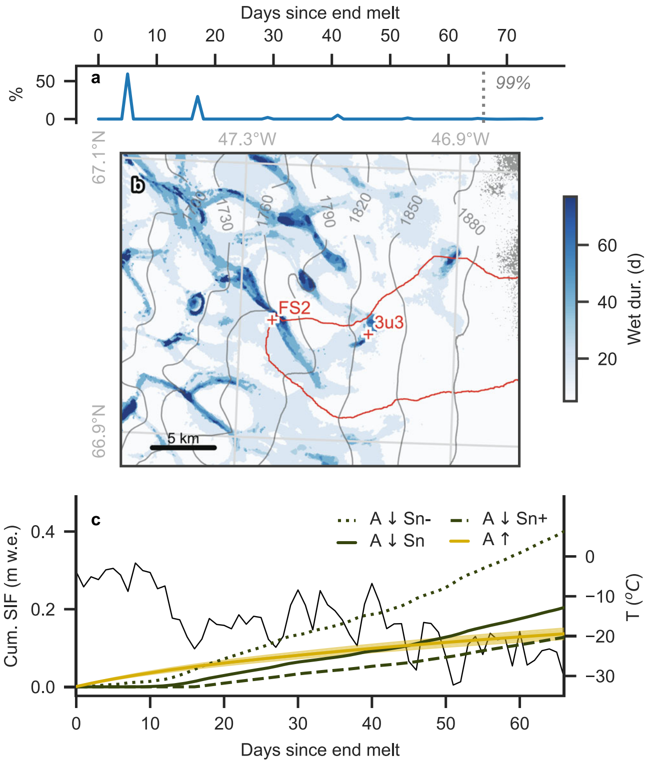

Fig. 4 | Superimposed ice formation (SIF) during autumn 2022. a, b Autumn residual wetness duration (days, d). **a** Histogram of panel b. 99th percentile shown by dashed line. **b** Map has same bounds as Fig. 1a, surface catchment of FS2 outlined in red, surface contours (m a.s.l.) in grey. **c** Cumulative autumn SIF. For top-down SIF (A↓, green), Sn-, Sn and Sn+ correspond to 0.3, 0.6 and 0.9 m snowpack thicknesses respectively. Bottom-up SIF (A↑) in yellow, shading shows range attributable to ± 1°C initial 10 m-depth temperature. Right axis: surface temperature (T, black line) used to calculate top-down SIF, from surface energy balance model (Methods). Source data are provided in Source Data files.

scenario (Fig. 5a), we examined model sensitivity using 1. 0 °C warmer (colder) initial 10 m depth temperatures based on ref. 28 firn temperature uncertainties for our study area, and 1.5× (0.5×) snowpacks, respectively (Fig. 5d). Across these scenarios, summer SIF is always the largest constituent of total SIF, while autumn bottom-up SIF is the next-largest component. Although the range in autumn top-down SIF associated with snowpack thickness is very large, it is a relatively small component of total SIF apart from in the thinnest snowpack scenario. The uncertainty in autumn SIF introduced by the radiometric sensitivity of the Sentinel-1 SAR sensor is low compared to our other sources of uncertainty (Fig. 5d thin vertical bars).

Considering the likely partitioning between retention and runoff at the visible runoff limit, our best-estimate scenario yields 84 % of total melt refrozen as SI, of which 65 % occurred during summer. The remaining 16 % of melt likely ran off via the surface river network passing by FS2 (Fig. 1c), though we cannot rule out subsequent refreezing at lower elevations. Considering the stronger SIF scenario (Fig. 5d, right), 105 % of total melt forms SIF, making this scenario unrealistic for our field area (SIF in excess of melt; precludes runoff, converse to indications from optical satellite imagery), while in the weaker SIF scenario (Fig. 5d, left) then only 71 % of melt is refrozen.

Superimposed ice formation across Greenland's ice slabs

We have established that refreezing onto ice slabs consists of at least two mechanisms: bottom-up SIF driven by slab cold content, and top-down SIF during autumn. A third mechanism is implicated by localised ice slab fractures that can enable melt to refreeze on the underside of the slabs[29] which we do not consider further here. Now we constrain at first order the importance of SIF onto the surface of ice slabs.

First we consider ice-slabs-wide autumn residual wetness. We used passive microwave radiometry[30] to identify the last day of the melt season (Methods). We used our SAR approach introduced above to identify the last wet day (Methods), yielding the annual duration of residual wetness (Fig. 6). Like in our field study area, residual wetness duration is effectively insensitive to the radiometric sensitivity of the Sentinel-1 SAR sensor, apart from minor sensitivity in 2022 (Suppl. Fig. 2). Residual wetness primarily varies according to the surface drainage network structure. On the western flanks remnants of slush fields and surface rivers are visible (Fig. 6b, c). Undrained lakes are particularly evident towards the lower slab extents. In the north and north-east, residual wetness is less pervasive and mainly consists of isolated wet patches (Fig. 6d, e), while in the south-east some residual wetness is detected around the upper margins of firn aquifers (Fig. 6a; ref. 12). The duration and extent of residual wetness around the annual visible runoff limit varied substantially by year (Suppl. Fig. 3), with more extensive and longer-duration wetness generally associated with a higher visible runoff limit. The western margins exhibited the most extensive wetness, extending over up to 80% of the area around the visible runoff limit in the several days following the end of the melt season, but as little as ~10 % in years when the visible runoff limit was lower than average. Extensive wetness can persist for up to roughly 30 days; beyond this, wetness tends to persist only in more isolated patches.

Next, we estimated summer and autumn SIF across the 'most likely', 'minimum' and 'maximum' ice slab extents[12]. For summer we used our SIF model in its bottom-up configuration, initialised with spatially-variable 10 m depth July firn temperatures (T_{10m})[28] (Methods). To assess the uncertainty associated with the initial temperature profiles, we also ran the model for the uncertainty bounds of T_{10m}. We determined the start of summer SIF by using the regional climate model MAR[3] to identify when surface melt first became available for SIF (Methods). In autumn, we used our wetness duration retrievals (excluding those areas which remained wet at the end of the calendar year, which are generally undrained supraglacial lakes) in conjunction with our model to estimate bottom-up and top-down SIF (Methods). We also considered the possibility of SIF due to top-down atmospheric cooling during colder summers with prolonged melt hiatuses. We found that at first order, this process can be neglected compared with the other modes of SIF production, so we do not consider it further (Supplementary Discussion).

Between 2017 and 2022 over the 'most likely' ice slab extents, summer top-down SIF occurred at an average rate of 7.2 (6.4–8.2) Gt yr^{-1} (Fig. 7b; bracketed values calculated from T_{10m} uncertainty bounds). On average autumn bottom-up SIF occurred at 1.2 (1.0–1.4) Gt yr^{-1} (Fig. 7c). Autumn top-down SIF is harder to assess because it is highly sensitive to the thickness of the snowpack overlying the slush matrix, yet this thickness cannot be adequately retrieved from MAR (Methods). In lieu we computed autumn top-down SIF under three fixed snow thicknesses: 0.5, 1.0 and 1.5 m, yielding on average 2.8, 0.9 and 0.4 Gt yr^{-1} respectively (Fig. 7d), so its maximum contribution is much less than half the average SIF which occurs in summer. Considering all SIF modes, total SIF occurred at 4.3, 9.3 or 11.6 Gt yr^{-1} across the minimum, most likely and maximum slab extents respectively when using predicted T_{10m} and a 1.0 m autumn snowpack.

Total SIF varied considerably between years (Fig. 7e). Over the 'most likely' slab extents, considering the high-melt year of 2019[31] SIF was divided between 5.3 Gt during the melt season and 2.3 Gt during autumn (assuming a 1.0 m snowpack), totalling 7.6 Gt. In contrast, 2022 was a more moderate melt year but with a large melt pulse in early September; 10.0 Gt SIF formed during the melt season and 2.3 Gt

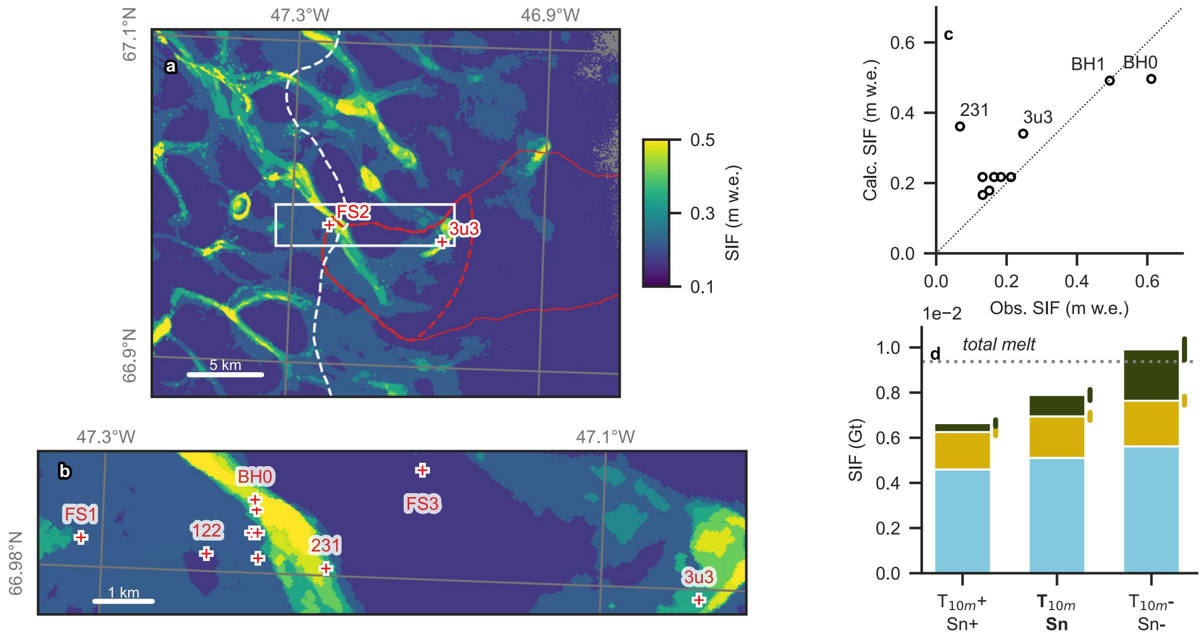

Fig. 5 | Superimposed ice formation (SIF) at the 2022 visible runoff limit. **a**–**c** Total SIF over field study area calculated using observed FS2 initial 10 m-depth temperature (T_{10m}) and an overlying autumn snowpack (Sn) of 0.6 m. **a** FS2's surface catchment (red), with 10 km limit (red dashes). 2022's visible runoff limit (white dashes). SIF measurement locations (red crosses). **b** Enlarged view of area indicated by white rectangle in panel **d**. **c** Comparison between observed and calculated SIF, with 1:1 line. **d** Analysis of SIF components in hydrological catchment up to 10 km limit. Autumn top-down: A↓; autumn bottom-up: A↑; summer bottom-up: S↑. The middle column corresponds to the `best-estimate' scenario (shown in panels **a**–**c**). The left column shows +1°C T_{10m} and 0.9 m snowpack; the right column −1°C T_{10m} and 0.3 m snowpack. Vertical bars denote the sensor uncertainty associated with detection of residual wetness duration. Dotted line shows the total net melt. Source data are provided in Source Data files.

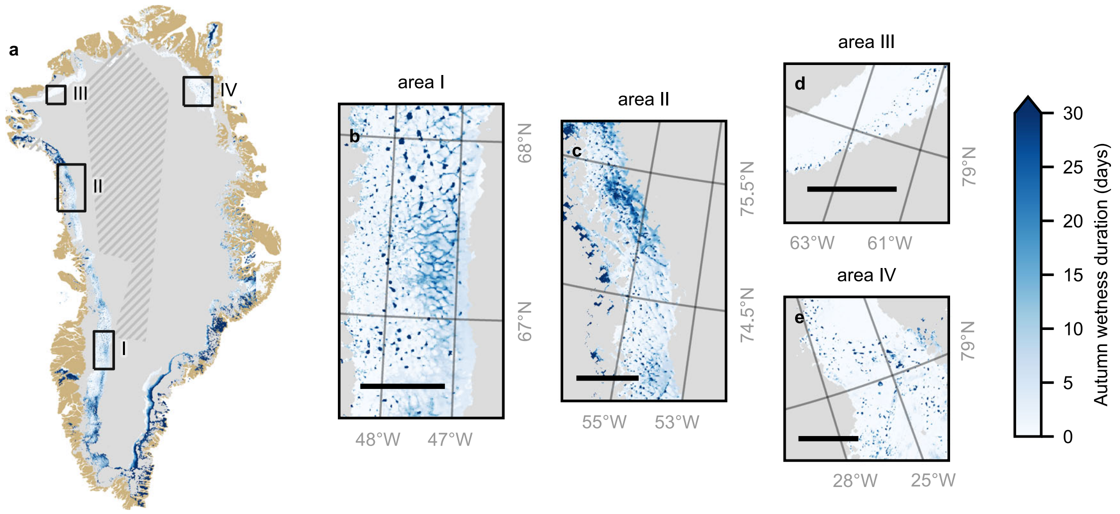

Fig. 6 | Ice-sheet-wide autumn wetness duration. Average residual wetness after the end of the melt season between 2017 and 2022 within the `maximum' ice slabs extent. **a** Ice-slabs-wide residual wetness. Ice sheet extent in grey, Greenland land mass in brown. Hatching indicates areas without SAR interferometric wide swath coverage. Boxes correspond to each area of interest. **b**–**e** Wetness in selected sectors. Scale bars (black) are 50 km long. **a**–**e** Contain modified Copernicus Sentinel-1 data [2017–2022].

in autumn, totalling 12.3 Gt, 57 % more than in 2019. This difference is caused mainly by summer SIF, which in 2019 was reduced because of the complete melting of seasonal snowpack up to elevations approaching the visible runoff limit. This caused some of the SIF which had formed earlier in the season to be re-melted, and highlights that SIF on ice slabs can only occur under moderate melt conditions. If melt removes all accumulation, exposing the slab itself to direct melting, then retention will be depleted, such as in the extraordinary melt year of 2012[32]. Such a reduction in slab retention during strong-melt summers will be accompanied by ice layer formation at elevations above existing slabs, laying the foundations for future slab expansion[11,33].

We quantified SIF by ice sheet drainage basin (Fig. 7f). Slabs along the western flank refroze the most meltwater, which is unsurprising given their large spatial extent. Despite sometimes extensive residual wetness, autumn refreezing accounts for at most one third of SIF in most basins, except the south-east, where autumn SIF apparently dominates; here, ref. 12 found possible ice slabs along the upper

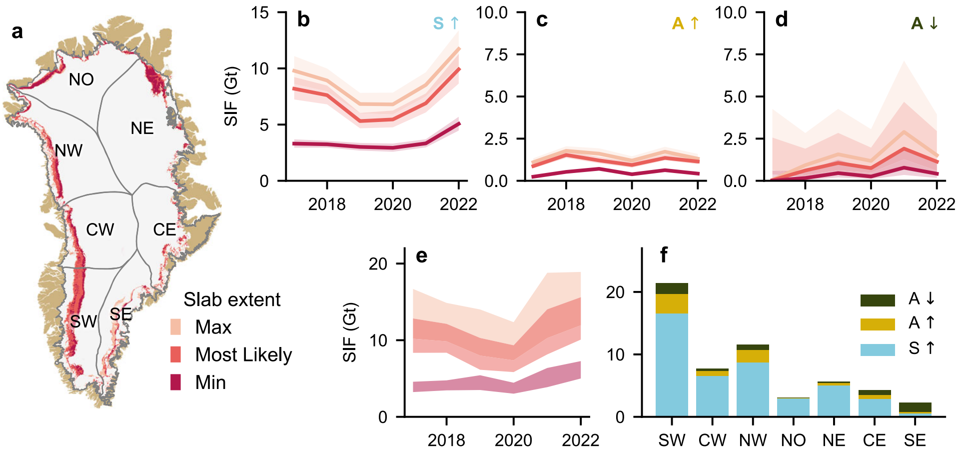

Fig. 7 | Superimposed ice formation (SIF) on ice slabs, 2017–2022. SIF divided into formation modes of summer bottom-up: S↑; autumn bottom-up: A↑; autumn top-down: A↓. **a** Ice slabs on the Greenland Ice Sheet according to ref. 12, classified into their `maximum', `most likely' and `minimum' extents, divided by drainage basin[59]. **b** Annual summer bottom-up SIF for each slab extent (colour-coded). Shading denotes uncertainty in the initial 10 m firn temperature (Methods). **c** Same as panel b but showing annual autumn bottom-up SIF. **d** Annual autumn top-down SIF for each slab extent (colour-coded). Shading denotes the range in SIF associated with the prescribed overlying snowpack between 0.5 and 1.5 m thick. **e** Total annual SIF ice-slabs-wide for each slab extent (colour-coded). For each slab extent minimum SIF is yielded by the warmest initial 10 m firn temperatures and thickest autumn snowpack, and maximum SIF is yielded by the coldest initial 10 m firn temperatures and thinnest autumn snowpack. **f** Total SIF by region, 2017-2022, using `most likely' slab extents, central initial 10 m firn temperatures and a 1 m-thick autumn snowpack, split into summer bottom-up, autumn bottom-up and autumn top-down components. Source data are provided in Source Data files.

margins of firn aquifers, which may be proto-aquifers with a similar tendency to refreeze residual water slowly over the autumn.

Discussion

Our in-situ measurements reveal SIF onto ice slabs in south-west Greenland simultaneously with visible surface hydrological features considered indicative of runoff. We can attribute SI to two distinct periods of formation. *(i)*. Summer SIF is governed by heat conduction to the underlying ice slab and occurs whenever liquid water is available at the slab surface. The rate slows through the melt season as the ice slab's cold content is consumed by latent heat release (Fig. 2c). Based on slab temperatures at the start of the 2022 melt season at FS2 (Fig. 2b) and observations made at KAN_U[8], we presume that most or all slab cold content can be replenished annually as a result of relatively low accumulation rates associated with slabs[34], consistent with ref. 18 and enabling background SIF to take place each melt season. *(ii)*. Autumn SIF is the smaller component of total SIF. It occurs in areas where water collects in the slush matrix. In-situ observations from the K-Transect in 2020 revealed water continuing to flow through the slush matrix over the slab after several days of frozen surface conditions[13], but without necessarily draining into surface rivers even though these can continue to flow for several days after the end of melting[35]. Our study shows that the largest SIF likely occurs where thin snowpack overlies autumn slush. We therefore presume that the most SIF occurs where the water table has risen to the surface and formed blue slush fields[35] that do not subsequently collapse into arterial river networks. Their lower albedo may further increase local meltwater availability and hence refreezing, an effect that we do not consider further here.

Our estimates of the percentage of melt which refreezes as SIF may appear reminiscent of retention capacities published by e.g.[4,7,36]. Those studies estimated refreezing in steady-state firn scenarios as percentages of accumulation. In contrast, we quantify SIF as a percentage of melt using measurements made under transient conditions. Direct comparisons to such studies are thus challenging. However, our findings shine new light on previous work to model retention by SIF, which in the context of scarce observations has remained essentially unvalidated. First, allowing for uncertainties in the density of the slush matrix (Supplementary Discussion), our in-situ measurements of total SIF at locations away from surface hydrological features are approximately half those modelled by[15]. Second, our modelling suggests that this SIF required roughly twice the amount of time to form compared to their model. Our thermistor string measurements show that the slab surface warms to roughly 0°C within days of the first occurrence of 0°C snowpack temperatures, which is a fundamental difference to maintaining a slab surface temperature between -5 and − 20°C as used by[15]. Our estimates of refreezing therefore suggest that previous attempts to model this process on glaciers substantially over-estimate SIF, even after we account for the spatially localised phenomenon of residual wetness refreezing during autumn and considering our model simplification that SIF occurs continuously throughout the melt season.

While we have made a first-order estimate of SIF onto Greenland's ice slabs, a full partitioning of meltwater's fate between retention and runoff on an ice-sheet-wide basis remains the domain of regional climate models with SMB schemes such as HIRHAM, MAR and RACMO[37]. However, their use of the skin layer formulation to calculate near-surface air temperature can cause an over-estimate of melt by a factor of two or three in the percolation zone[38]. Thus, we do not attempt to estimate ice-slabs-wide runoff as the residual of modelled melt minus refreezing. Instead, considering runoff estimated from CryoSat-2 satellite altimetry between 2011 and 2020 of 357 ± 58 Gt yr^{-1} (ref. 39), our average rate of 9.3 Gt yr^{-1} SIF over the 'most likely' extent of ice slabs implies that SIF on slabs reduces annual total ice-sheet-wide runoff by 2-3%.

SMB projections by regional climate models indicate that the ice sheet's refreezing trajectory will depend strongly on the climate scenario[40]. Under the strongest climate warming scenarios and even without allowing for ice slab development (i.e. maximum rather than minimum pore-space fill-in time[4]), peak refreezing of the ice sheet could be reached as early as the 22nd century, but under intermediate warming then refreezing at higher elevations of the ice sheet is projected to plateau instead. Here, the hypsometry of the ice sheet has both positive and negative effects. Its flatness towards higher elevations will enable runoff areas to expand disproportionately with warming[10,25], but this same flatness is also likely to delay the evacuation of water through the slush matrix to discharge into surface rivers. This would result in more SIF than we observed and hence suppress runoff from the vicinity of the visible runoff limit even more than during the time period of this study. Signs of such behaviour are already detectable in years when the visible runoff limit approaches contemporary maxima, as vast slush fields form which tend to result in longer autumn wetness.

Overall our findings reveal that while Greenland's ice slabs now often undergo visible surface runoff[10], substantial quantities of melt can concurrently be converted to superimposed ice as the wet slush matrix overlying the slab refreezes from the bottom up and top down. At the 2022 runoff limit in south-west Greenland, we found that around 84% of the melt available for runoff instead most likely refroze as SIF onto the underlying ice slab, a value which presumably decreases downstream as melt increases and more surface rivers form. Some melt refroze in-situ, directly beneath where it was produced, while some melt started to flow laterally but subsequently refroze some kilometres downstream. Ice-slabs-wide, we estimate that ice slabs refroze around 56 Gt of melt as superimposed ice between 2017 and 2022 ('most likely' extents; 26 Gt and 69 Gt at minimum and maximum extents respectively), of which roughly 78 % was by refreezing during the melt season and the remainder by during autumn. SIF by consumption of ice slab cold content dominates total SIF, despite substantial uncertainties in how much SIF occurs by atmospheric cooling during autumn.

The cold content of ice slabs acts together with shallow surface slopes to inhibit rapid surface water drainage, making slabs hotspots of refreezing during the melt season and into autumn. However, during very strong melt seasons, all seasonal snowpack and firn protecting the slabs from direct melting can disappear, subjecting the slab surface to surface hydrological processes reminiscent of the ablation zone. This suggests that contemporary slabs will reach an upper thickness beyond which they transition to ablation areas, but that at higher elevations new slabs will continue to expand upslope and thicken under all but the most extreme warming scenarios.

Methods

Surface hydrological catchments

We used SAGA GIS[41] to delineate the hydrological catchments of our field sites FS1, FS2, and FS3 from ArcticDEM[42] to the uppermost limits of the underlying ice slab[11]. The surface catchments of FS1 and FS3 are very small (1.1 and 0.1 km^2 respectively), so we considered the catchment area upstream of FS2 only, which has an area up to the ice slab limits of 175 km^2.

Measuring in-situ superimposed ice formation

In April 2021 (before the melt season) we dug pits and buried metal meshes to set marker horizons at three locations (Fig. 1a). In April 2022 we returned to measure ice formation on top of them by digging down to the new ice slab surface and then using an auger to drill into the ice until metal chips appeared at the top of the hole. This method is subject to uncertainties which are likely several centimetres of underestimation, in particular at FS3 where we had difficulties determining the April 2021 slab surface without destroying it due to the presence of mixed firn and ice lenses on top of the slab.

Between April 2022 and April 2023, we instead employed a repeat shallow core method at eleven locations. Using a Kovacs Mark II coring system, we drilled a 9 cm diameter core from the surface down through the snow and any firn (if present), until approximately 0.5 m into the slab (Suppl. Fig. 1a). We measured the depth of the borehole independently of the retrieved core length to check for core collapsing. One third of the cores had short collapsed sections, on average 6 cm long (max. 10 cm) and always situated in brittle depth hoar. We noted the core stratigraphy and measured density at 10 cm resolution. For the collapsed sections, we used the average measured density of depth hoar. We then fixed a bamboo stake in direct contact with the ice at the base of the borehole and measured the length of the stake which remained exposed (Suppl. Fig. 1b). One year later we revisited each site, that is the location of the stake which had moved due to ice flow (~60 m yr^{-1} in the study area). We measured the distance from the top of the stake to the snow surface. Then we repeated the drilling in close vicinity of the stake (<1 m; Suppl. Fig. 1c) and we again noted stratigraphy, measured densities at 10 cm resolution and measured the depth of the hole independently of the core. Key parameters in the density measurements such as core diameter were checked throughout logging.

We used the top of each stake to align the two density profiles (Suppl. Fig. 1d) to (i) quantify SIF in metres as well as metres water equivalent, and (ii) quantify local climatic surface mass balance (cSMB). The latter was calculated by directly subtracting the water equivalent measured in spring one and spring two. For the purpose of the subtraction, water equivalent was summed up over the depth range from the snow surface in year two down to the ice slab surface in year one.

We drilled repeat cores, which indicated that our measurements were repeatable and that metres scale variability in SIF was negligible (Supplementary Discussion). We also considered the impact of springtime densification on SIF as a potential source of systematic errors (Supplementary Discussion).

Measuring slab temperatures

At FS2, in May 2022 we installed a 12 m digital temperature chain with 34 sensors, with spacing increasing from 0.15 m at the top of the chain to 1 m at the bottom (*beadedstream, inc*). The chain was installed in a borehole of ~ 11 cm diameter drilled by a Kovacs Mark II coring system and suspended from a boom attached to a mast frozen into the subsurface. This enabled us to capture not only slab temperatures but also seasonal snowpack temperatures with respect to a fixed datum. Measurements were logged on a D605 logger (*beadedstream, inc*) every 15 minutes until recording stopped unexpectedly on 18 September at 04:00 UTC.

Melt available for runoff or SIF in field area

We calculated meltwater production in our study area using a surface energy balance/surface mass balance (SEB/SMB) model forced by local observations from three weather stations, including KAN_U, supplemented with MODIS albedo[25]. The SEB/SMB model calculates surface energy and mass balance components in 100 m elevation bins.

The model's sub-surface scheme (0.25 m resolution) consists of a seasonal snowpack overlying firn and ice layers generated since the model initialisation in spring 2009. The model calculates surface melt refreezing in underlying layers with pore space and cold content. At the start of the melt season, meltwater refreezes locally, warming and densifying the snowpack, and no runoff occurs. Once the overlying snowpack is isothermal then water percolates down to the underlying modelled ice layers, which are defined as impermeable when >1 m thick. They are present throughout our study's elevation range, causing instantaneous runoff. We therefore estimate the meltwater available for SIF or runoff as that produced between the start of modelled runoff and the end of the melt season, less the refreezing at 0.25 m depth which captures diurnal refreezing as the near-surface cools at night.

We assessed model performance by comparison with observations of surface lowering at FS1, FS2 and FS3 which were each equipped with a CR1000X datalogger (*Campbell Scientific; CS*) and a CS SR50A sonic ranger mounted on a horizontal boom roughly 1–2 m above the snow to measure surface height changes. In 2022 at 1800 m a.s.l., the model produced 0.25 m w.e. melt available for runoff or SIF. This is in excellent agreement with our observations: using a fixed summer-time density of 504 kg m^{-3} (ref. 13) to convert surface lowering to water equivalent, 0.23 to 0.27 m w.e. melt occurred in the same time period.

To interpolate melt available for runoff or SIF in 2022 over our hydrological catchment we used linear regression between elevation and melt modelled in the 100 m elevation bins between 1600 and 1,900 m (R^2 = 0.99, p < 0.01, n = 4) to map melt production as a function of elevation.

Modelling superimposed ice formation

There have been limited previous efforts to simulate SIF by slush refreezing on top of an ice slab, principally addressing only bottom-up refreezing and neglecting any impact of lateral flow of meltwater[15,43,44]. The model by ref. 45 addresses the effect of lateral meltwater flow in SIF but lacks top-down refreezing and uses an experimental flow-line approach. Most regional climate models (RCMs) applied to the Greenland Ice Sheet do not have an ability to simulate slush and they are all restricted to 1D simulations along the depth axis. Lateral flow of meltwater and ponding, important in autumn SIF, therefore cannot be simulated. Furthermore, RCM simulated firn structure and firn temperatures in the lower accumulation area, essential to reliably simulate SIF, are of limited accuracy[28,46]. In summary there are currently no models suitable to simulate SIF on an ice-sheet-wide scale.

We aimed to make a first-order estimate of Greenland-wide SIF on ice slabs and to assess the relative importance of bottom-up and top-down SIF. We do not claim to capture the full complexity of the processes involved. Here we describe the model formulation and its application to our field study area. Its ice-slabs-wide application is described separately in 'Ice-slabs-wide wetness and superimposed ice formation', below.

Our 1-dimensional heat flow model computes SIF based on the amount of latent heat evacuated from slush. The heat flux follows the temperature gradient between the slush (0°C) and the cold slab in the case of bottom-up refreezing, or between the slush and cold snow during top-down refreezing (Fig. 3). We assume that heat conduction is the only mechanism of heat flux. Heat conduction is calculated numerically in time steps of 200 seconds and along the depth axis in 10 cm layers. We use a density of 920 kg m^{-3} for ice and a density of 400 kg m^{-3} for snow with a porosity of 0.4 and 5% initial irreducible water content. This value of irreducible water content is located between the classical value of 7 % indicated by ref. 47 and values used in regional climate models, such as MAR where it varies with depth from 7% at the surface to 2% at 1 m below the surface. Thermal conductivity was set to 2.25 W m^{-1} K^{-1} for ice and 0.5 W m^{-1} K^{-1} for snow at 400 kg m^{-3} (refs. 48,49). We used a specific heat capacity of ice of 2090 J kg^{-1} K^{-1} and latent heat of 334,000 J kg^{-1}.

To model bottom-up SIF we assume that there is always slush at 0 °C on top of the impermeable ice slab. Slush is continuously refrozen as its latent heat is released and conducted to the ice slab. Temperatures at the bottom of the model domain are allowed to fluctuate without prescribing a fixed bottom heat flux; at every time step, the temperature change of the bottom-most grid cell equals the temperature change in the cell above. We specified our bottom-up model domain and initialisation according to thermistor string measurements acquired at FS2, where the slab is >12 m thick[13]. The model domain was 12 m deep, with the interface between slush and ice slab located at 0 m depth. The model was initialised with a measured firn temperature profile from 6 July 2022 14:15 UTC, the moment where the thermistor closest to the ice slab surface reached ~0°C. After initialisation, the model ran independently of measured firn temperatures. We then partitioned bottom-up SIF into its summer and autumn components according to the last day of the summer melt season and the last day of residual wetness (according to SAR acquisitions, below).

We model top-down SIF separately to bottom-up SIF, for two major reasons. First, the thickness of the slush layer is unknown, especially during autumn when both processes of SIF are active at the same time. By modelling the two processes separately, we avoid the need to prescribe the slush layer thickness. Second, the snowpack overlying the layer of slush is also poorly constrained (Fig. 3). In our field study area we evaluated the sensitivity of the model results to snowpack thickness overlying slush by running our calculations for the observed snowpack thickness of 0.6 m as well as snowpacks 0.5 × and 1.5 × thinner and thicker respectively. Initial irreducible water content froze as the cold wave moved through the snowpack. The top model boundary was taken to be the snow surface where the temperature therefore varied according to the surface temperatures calculated by the SEB/SMB model. The bottom boundary was fixed at 0°C. Model runs started following the last day of surface melting and ended on the last day of residual wetness.

Remote sensing of autumn residual wetness

Theoretical radar backscatter response to sub-surface meltwater. Horizontally-transmitted, vertically-received (HV) backscatter intensity observations (hereafter σ_0^{HV}) made by 5.4 GHz radar are highly sensitive to the dielectric contrast between water and snow/ice and penetrate up to a few metres of ice under dry conditions[50]. σ_0^{HV} is therefore indicative of water content in the uppermost metres of the near-surface snow and firn.

To further verify the suitability of our approach to detect sub-surface wetness we carried out a suite of radiative transfer (RT) modelling experiments in the Snow Microwave Radiative Transfer (SMRT) model[51] using the sticky hard sphere (SHS) model (Supplementary Methods). Our results indicate that variability in the liquid water content of the sub-surface layer dominates the reduction in the modelled σ_0^{HV} (Supplementary Discussion).

Synthetic Aperture Radar data. We used Synthetic Aperture Radar (SAR) backscatter intensity data acquired by the European Space Agency Sentinel-1 platform. Data availability prior to 2017 is insufficient for this study. Since 2017/2018 the acquisition strategy favours more frequent data acquisition. We used Interferometric Wide mode σ_0^{HV} data, delivered as a ground-range-detected (GRD) product at 25 m resolution. Acquisitions were more frequent from 2017 until the end of 2021 when Sentinel-1B failed. All data were pre-processed following standard procedures (Supplementary Methods).

Detecting residual water presence. We detected residual water in the upper several metres of the snow/firn/ice column following the end of the melt season until the end of the calendar year by examining successive autumn SAR acquisitions co-normalised by subtracting winter reference scenes of the corresponding satellite orbit to yield $\widehat{\sigma}_0^{HV}$ (ref. 27). This approach reduces variations in σ_0^{HV} introduced by observation geometry, terrain fluctuations and melt conditions between images acquired at different times. Moreover, it allows to account for spatial variations in surface and subsurface heterogeneities (e.g. surface roughness, sastrugi, ice lenses, ice pipes, percolation pipes) that affect the spatial variations in σ_0^{HV}. Therefore, we assume that these heterogeneities are temporally non-varying, such that changes in the cross-polarization backscatter can be attributed solely to changes in dielectric permittivity rather than surface roughness and volume scattering[52].

We generated a winter reference scene for each orbit by calculating the median of all data acquired between 1 March and 16 April each year between 2017 and 2022. Next, we co-normalised scenes acquired between July and December each year using the corresponding reference scene. When the snow/firn column is completely frozen the $\widehat{\sigma}_0^{HV}$ distribution is zero-centred with little variance (Suppl. Fig. 4, green curve). Conversely, when water is present in the column it can be detected as an anomaly relative to background $\widehat{\sigma}_0^{HV}$ (Suppl. Fig. 4, purple curve.).

To identify the threshold at which $\widehat{\sigma}_0^{HV}$ pixels can be considered wet we used the 1st percentile of $\widehat{\sigma}_0^{HV}$ in May 2021 (i.e. prior to surface melting) across all ice slabs as mapped by[12] (Suppl. Fig. 4, green curve). We added the Sentinel-1's radiometric sensitivity of -1 dB, yielding a wetness detection threshold T_{wet} <−2.17 dB (Suppl. Fig. 4, blue vertical line). To evaluate uncertainty in our wetness durations we varied our threshold by ± 0.3 dB, which is the stated 1σ precision of the Sentinel-1 sensor[53].

Ice-slabs-wide wetness and superimposed ice formation

Ice slabs extent. We used observationally-derived ice slab extents at 500 m resolution[12]. This data product distinguishes between the 'most likely', 'minimum' and 'maximum' slab extents. We estimated SIF over each of these extents during the period 2017 to 2022.

Identifying the end of the melt season. Passive microwave radiometry (PMR) is widely adopted to detect surface melting over the Greenland Ice Sheet. We used Ka band (37 GHz) horizontally polarized brightness temperatures measured on a daily basis by the SSMI/S-F17 sensor and binned at a spatial resolution of 3.125 km[54]. At this frequency PMR interacts with the uppermost few centimetres of the ice sheet surface and is thus indicative purely of surficial water status. Surface melting is detected for a pixel when the measured brightness temperature is higher than a threshold value. The threshold is dynamically computed for each pixel and for every year according to the simulations of a microwave emission model[30]. We considered all data up to 30 September each year. In each pixel we identified the last day of surface melting each year.

Autumn residual wetness. We defined the residual wetness duration as between the end of surface melting (PMR) and the last date of residual wetness (SAR).

We analysed ascending and descending orbits of Sentinel-1 separately. We preferentially used data from ascending orbits to mitigate against conflicting geo-location errors present in the Google Earth Engine version of the Sentinel-1 data (Supplementary Methods). This approach limits the temporal resolution to the relative orbit of the chosen orbit direction: 5 days when Sentinel-1B was active, otherwise 11 days. We multi-looked to 500 m resolution, matching the ice slab extents dataset.

We excluded two short periods of SAR data as follows: 26 Nov 2021 and 28–31 Oct 2022. During both these periods temperatures rose briefly to ~0 °C, causing identification of surface melting which was not indicative of multi-day sub-surface wetness. The snowpack had already undergone several weeks of atmospheric cooling, making it highly likely that any surface melt refroze in the upper snowpack before it could reach the slab surface.

Bottom-up SIF. We calculated the slab-wide amount of bottom-up SIF in summer and autumn by running our 1-D heat flow model over the 10 km grid of the regional climate model MAR and then resolving the end of residual wetness using SAR measurements at 500 m resolution.

To simplify computation over all ice slabs and because the slabs extent dataset by ref. 12 does not also provide slab thickness, we assumed that slabs are 12 m thick like at FS2. This value is roughly in the middle of the observed ice-sheet-wide slabs thickness range: well-developed slabs have a median thickness of 15 m, while slabs in development or initiation have a median thickness of around 5–11 m[11]. We checked the sensitivity of our model to slab thickness by repeating the model run at FS2 (Fig. 2) with slab thicknesses of 5 and 15 m. Over this thickness range, SIF at the end of the melt season on 18 September varied by <2 mm w.e. and so we conclude that prescribing slab thickness of 12 m has a negligible impact on our results.

We specified the initial slab temperature profile in each grid cell based on observation-derived monthly 10 m firn temperatures (T_{10m}) interpolated across the ice sheet at 0.1° resolution[28]. We used this dataset to scale our initialisation profile measured at FS2 so that T_{10m} agreed with the closest value $T_{10\mathrm{m\ local}}$ in July each year. Temperatures at all depths were then multiplied by $T_{10\mathrm{m\ local}}/T_{10\mathrm{m\ FS2}}$ which preserves the condition of 0°C at the top of the ice slab. To assess the sensitivity of bottom-up SIF to the initial temperature profile, we ran the model using T_{10m} ± their associated per-pixel uncertainty estimate.

The simulation period was individual to each grid cell. The simulation commenced when meltwater was inferred to percolate to the top of the slab for the first time. This date is logically always some time after surface melt begins, so we cannot use PMR for this purpose. Instead we used MAR v3.14.0[37] forced by ERA-5[55] to identify the date on which modelled runoff from beneath the seasonal snowpack commenced. MAR simulates solid ice layers below seasonal snowpack in all ice slab areas and modelled runoff therefore begins once meltwater has warmed the snowpack and percolated down to the ice layer.

In principle the bottom-up SIF attributable to summer ceases at the end of the melt season determined by PMR. However, we also needed to account for the possibility that the snowpack melts away before the end of the melt season, exposing the slab at the surface, which can be relevant towards the lower elevations of slabs. If a cell became snow-free according to MAR then we halted summer-time bottom-up SIF accordingly and subtracted any subsequent melting from the already-formed SI.

We calculated autumn bottom-up SIF by allowing the bottom-up model to continue into autumn beyond the end of surface melting for as long as residual wetness determined by SAR (at 500 m resolution) was present.

Top-down SIF. Like bottom-up SIF we ran the top-down SIF model over the MAR grid. We initialised the model with an isothermal 0°C snowpack with 5% irreducible water content then forced it with MAR v3.14.0 surface temperatures at the topmost snow layer in each numerical time step. As soon as subzero temperatures reached the snow-to-slab interface then top-down SIF could begin.

In each cell the simulation started the day after the end of the melt season according to PMR. We ran the simulation until the end of the year. Then, we used the residual wetness duration measured by SAR to determine the end of top-down SIF at 500 m resolution. The thickness of the overlying snowpack was held constant, which means that snowfall events were not included. We considered using MAR end-of-season snowpack thicknesses but found them to be spatially incoherent, so instead we investigated SIF under 0.5, 1.0 and 1.5 m of overlying snowpack to provide bounds on model sensitivity.

Top-down autumn SIF is likely to be more complicated than our first-order simplified approach. For instance, although rarely observed, slush fields can suddenly appear at the surface during cold periods, which may have similarities to aufeis formation in Arctic terrain[56–58]. Further consideration is beyond the scope of the present study.

Data availability

Source data are provided with this paper. Field data and the outputs from this study are available at https://doi.org/10.5281/zenodo.15089547. ArcticDEM was provided by the Polar Geospatial Center (https://www.pgc.umn.edu/data/arcticdem/). Melt and runoff outputs from the SEB/SMB model used in our study area are available in our main repository. The weather station data underlying the SEB/SMB model outputs are available from the Programme for Monitoring of the Greenland Ice Sheet (https://promice.org/). Sentinel-1 and Sentinel-2 data are acquired by the Copernicus Programme of the European Space Agency. These data were either downloaded from the Alaska Satellite Facility Distributed Active Archive Center (https://asf.alaska.edu) or processed within Google Earth Engine (https://earthengine.google.com). Passive Microwave Radiometry data can be retrieved from the National Snow and Ice Data Center (https://nsidc.org/data/nsidc-0630/). MAR outputs are available at http://ftp.climato.be/fettweis. Ice slab extents are available at https://doi.org/10.5281/zenodo.10892397. Firn 10 m temperatures are available at https://doi.org/10.22008/FK2/TURMGZ. Ice sheet drainage divides are available at https://doi.org/10.7280/D1WT11. The outline of Greenland was provided by Natural Earth (https://www.naturalearthdata.com/). Source data are provided with this paper.

Code availability

Analysis scripts are available at https://doi.org/10.5281/zenodo.15089547. The Snow Microwave Radiative Transfer Model is available at https://smrt-model.science/ and was run using the code available at https://colab.research.google.com/drive/1DH6btbeiBTrM3fCByihu4LlFYC79ADuP.

References

1. van Angelen, J. H., Lenaerts, J. T. M., van den Broeke, M. R., Fettweis, X. & van Meijgaard, E. Rapid loss of firn pore space accelerates 21st century Greenland mass loss. *Geophys. Res. Lett.* **40**, 2109–2113 (2013).
2. Steger, C. R., Reijmer, C. H. & van den Broeke, M. R. The modelled liquid water balance of the Greenland Ice Sheet. *Cryosphere* **11**, 2507–2526 (2017).
3. Fettweis, X. et al. Reconstructions of the 1900–2015 Greenland Ice Sheet surface mass balance using the regional climate MAR model. *Cryosphere* **11**, 1015–1033 (2017).
4. Pfeffer, W. T., Meier, M. F. & Illangasekare, T. H. Retention of Greenland runoff by refreezing: Implications for projected future sea level change. *J. Geophys. Res.* **96**, 22117 (1991).
5. Harper, J., Humphrey, N., Pfeffer, W. T., Brown, J. & Fettweis, X. Greenland ice-sheet contribution to sea-level rise buffered by meltwater storage in firn. *Nature* **491**, 240–243 (2012).
6. The IMBIE Team. Mass balance of the greenland ice sheet from 1992 to 2018. *Nature* **579**, 233–239 (2019).
7. Braithwaite, R. J., Laternser, M. & Pfeffer, W. T. Variations of near-surface firn density in the lower accumulation area of the Greenland ice sheet, Pakitsoq, West Greenland. *J. Glaciol.* **40**, 477–485 (1994).
8. Machguth, H. et al. Greenland meltwater storage in firn limited by near-surface ice formation. *Nat. Clim. Change* **6**, 390–393 (2016).
9. MacFerrin, M. et al. Rapid expansion of Greenland's low-permeability ice slabs. *Nature* **573**, 403–407 (2019).
10. Tedstone, A. J. & Machguth, H. Increasing surface runoff from Greenland's firn areas. *Nat. Clim. Change* **12**, 672–676 (2022).
11. Jullien, N., Tedstone, A. J., Machguth, H., Karlsson, N. B. & Helm, V. Greenland Ice Sheet ice slab expansion and thickening. *Geophys. Res. Lett.* **50**, e2022GL100911 (2023).
12. Culberg, R., Michaelides, R. J. & Miller, J. Z. Sentinel-1 detection of ice slabs on the Greenland Ice Sheet. *Cryosphere* **18**, 2531–2555 (2024).
13. Clerx, N. et al. In situ measurements of meltwater flow through snow and firn in the accumulation zone of the SW Greenland Ice Sheet. *Cryosphere* **16**, 4379–4401 (2022).
14. Smith, L. C. et al. Efficient meltwater drainage through supraglacial streams and rivers on the southwest Greenland ice sheet. *Proc. Natl Acad. Sci. USA* **112**, 1001–1006 (2015).
15. Bøggild, C. E. Simulation and parameterization of superimposed ice formation. *Hydrol. Process.* **21**, 1561–1566 (2007).
16. Reijmer, C. H., van den Broeke, M. R., Fettweis, X., Ettema, J. & Stap, L. B. Refreezing on the Greenland Ice Sheet: a comparison of parameterizations. *Cryosphere* **6**, 743–762 (2012).
17. Cox, C., Humphrey, N. & Harper, J. Quantifying meltwater refreezing along a transect of sites on the Greenland Ice Sheet. *Cryosphere* **9**, 691–701 (2014).
18. Bøggild, C. E., Forsberg, R. & Reeh, N. Meltwater retention in a transect across the Greenland Ice Sheet. *Ann. Glaciol.* **40**, 169–173 (2005).
19. Humphrey, N. F., Harper, J. T. & Pfeffer, W. T. Thermal tracking of meltwater retention in Greenland's accumulation area. *J. Geophys. Res.: Earth Surf.* **117** (2012).
20. Wright, A. P. et al. Modeling the refreezing of meltwater as superimposed ice on a high Arctic glacier: A comparison of approaches. *J. Geophys. Res.* **112** (2007).
21. Wadham, J. L. & Nuttall, A.-M. Multiphase formation of superimposed ice during a mass-balance year at a maritime high-Arctic glacier. *J. Glaciol.* **48**, 545–551 (2002).
22. Baird, P. D. Part i: Method of nourishment of the Barnes ice cap. *J. Glaciol.* **2**, 2–9 (1952).
23. Koerner, R. M. Some observations on superimposition of ice on the Devon Island ice cap, N.W.T. Canada. *Geografiska Annaler: Ser. A, Phys. Geogr.* **52**, 57–67 (1970).
24. van de Wal, R. S. W. et al. Twenty-one years of mass balance observations along the K-transect, west Greenland. *Earth Syst. Sci. Data* **4**, 31–35 (2012).
25. van As, D. et al. Hypsometric amplification and routing moderation of Greenland Ice Sheet meltwater release. *Cryosphere* **11**, 1371–1386 (2017).
26. Brangers, I. et al. Sentinel-1 detects firn aquifers in the Greenland Ice Sheet. *Geophys. Res. Lett.* **47**, e2019GL085192 (2020).
27. Liang, D. et al. Time-series snowmelt detection over the Antarctic using Sentinel-1 SAR images on Google Earth Engine. *Remote Sens. Environ.* **256**, 112318 (2021).
28. Vandecrux, B. et al. Recent warming trends of the Greenland Ice Sheet documented by historical firn and ice temperature observations and machine learning. *Cryosphere* **18**, 609–631 (2024).
29. Culberg, R., Chu, W. & Schroeder, D. M. Shallow fracture buffers high elevation runoff in northwest Greenland. *Geophys. Res. Lett.* **49**, e2022GL101151 (2022).
30. Colosio, P., Tedesco, M., Ranzi, R. & Fettweis, X. Surface melting over the Greenland Ice Sheet derived from enhanced resolution passive microwave brightness temperatures (1979-2019). *Cryosphere* **15**, 2623–2646 (2020).
31. Tedesco, M. & Fettweis, X. Unprecedented atmospheric conditions (1948-2019) drive the 2019 exceptional melting season over the Greenland Ice Sheet. *Cryosphere* **14**, 1209–1223 (2019).
32. Mikkelsen, A. B. et al. Extraordinary runoff from the Greenland Ice Sheet in 2012 amplified by hypsometry and depleted firn retention. *Cryosphere* **10**, 1147–1159 (2016).
33. Culberg, R., Schroeder, D. M. & Chu, W. Extreme melt season ice layers reduce firn permeability across Greenland. *Nat. Commun.* **12**, 2336 (2021).
34. Brils, M. et al. Climatic drivers of ice slabs and firn aquifers in Greenland. *Geophys. Res. Lett.* **51**, e2023GL106613 (2024).
35. Holmes, C. W. Morphology and hydrology of the Mint Julep area, southwest Greenland. In *Project Mint Julep Investigation of Smooth Ice Areas of the Greenland Ice Cap, 1953; Part II Special Scientific Reports* (Project Mint Julep Investigation of Smooth Ice Areas of the Greenland Ice Cap, 1953; Part II Special Scientific Reports, 1955).
36. Reeh, N. Parameterization of melt rate and surface temperature on the Greenland Ice Sheet. *Polarforschung* **59**, 113–128 (1991).
37. Fettweis, X. et al. GrSMBMIP: intercomparison of the modelled 1980–2012 surface mass balance over the Greenland Ice Sheet. *Cryosphere* **14**, 3935–3958 (2020).
38. Covi, F., Hock, R. & Reijmer, C. H. Challenges in modeling the energy balance and melt in the percolation zone of the Greenland Ice Sheet. *J. Glaciol.* **69**, 164–178 (2023).
39. Slater, T. et al. Increased variability in Greenland Ice Sheet runoff from satellite observations. *Nat. Commun.* **12**, 6069 (2021).
40. Noël, B., Lenaerts, J. T. M., Lipscomb, W. H., Thayer-Calder, K. & van den Broeke, M. R. Peak refreezing in the Greenland firn layer under future warming scenarios. *Nat. Commun.* **13**, 6870 (2022).
41. Conrad, O. et al. System for automated geoscientific analyses (SAGA) v. 2.1.4. *Geosci. Model Dev.* **8**, 1991–2007 (2015).
42. Porter, C. et al. ArcticDEM, version 3. https://doi.org/10.7910/DVN/3VDC4W.
43. Obleitner, F. & Lehning, M. Measurement and simulation of snow and superimposed ice at the Kongsvegen glacier, Svalbard (Spitzbergen). *J. Geophys. Res. Atmos.* **109**, D04106 (2004).

44. Langen, P. L., Fausto, R. S., Vandecrux, B., Mottram, R. H. & Box, J. E. Liquid water flow and retention on the Greenland Ice Sheet in the regional climate model HIRHAM5: Local and large-scale impacts. *Front. Earth Sci.* **4**, 110 (2017).
45. Clerx, N., Machguth, H., Tedstone, A. & van As, D. Modelling lateral meltwater flow and superimposed ice formation atop Greenland's near-surface ice slabs. *J. Glaciol.* **70**, e54 (2024).
46. Machguth, H. et al. Runoff from Greenland's firn area - why do MODIS, RCMs and a firn model disagree? *EGUsphere* [preprint], https://doi.org/10.5194/egusphere-2024-2750 (2024).
47. Colbeck, S. C. Water flow through snow overlying an impermeable boundary. *Water Resour. Res.* **10**, 119–123 (1974).
48. Calonne, N. et al. Numerical and experimental investigations of the effective thermal conductivity of snow. *Geophys. Res. Lett.* **38**, L23501 (2011).
49. Calonne, N. et al. Thermal conductivity of snow, firn, and porous ice from 3 d image based computations. *Geophys. Res. Lett.* **46**, 13079–13089 (2019).
50. Rignot, E., Echelmeyer, K. & Krabill, W. Penetration depth of interferometric synthetic-aperture radar signals in snow and ice. *Geophys. Res. Lett.* **28**, 3501–3504 (2001).
51. Picard, G., Sandells, M. & Löwe, H. SMRT: an active–passive microwave radiative transfer model for snow with multiple microstructure and scattering formulations (v1.0). *Geosci. Model Dev.* **11**, 2763–2788 (2018).
52. Rignot, E. Backscatter model for the unusual radar properties of the Greenland Ice Sheet. *J. Geophys. Res. Planets* **100**, 9389–9400 (1995).
53. Geudtner, D. & Torres, R. Sentinel-1 system overview and performance. In *IEEE International Geoscience and Remote Sensing Symposium* (IEEE 2012).
54. Brodzik, M., Long, D., Hardman, A., Paget, A. & Armstrong, R. Measures calibrated enhanced-resolution passive microwave daily EASE-grid 2.0 brightness temperature esdr, version 1 (2025).
55. Hersbach, H. et al. The ERA5 global reanalysis. *Q. J. R. Meteorol. Soc.* **146**, 1999–2049 (2020).
56. Kane, D. L. Physical mechanics of aufeis growth. *Can. J. Civ. Eng.* **8**, 186–195 (1981).
57. Schohl, G. A. & Ettema, R. Theory and laboratory observations of naled ice growth. *J. Glaciol.* **32**, 168–177 (1986).
58. Turcotte, B., Dubnick, A., McKillop, R. & Ensom, T. Icing and aufeis in cold regions i: the origin of overflow. *Can. J. Civ. Eng.* **51**, 93–108 (2023).
59. Mouginot, J. & Rignot, E. Glacier catchments/basins for the Greenland Ice Sheet. https://doi.org/10.7280/D1WT11 (2019).

Acknowledgements

This study was supported by European Research Council award 818994 – Cassandra (AT, HM, NC and NJ), the Swiss National Science Foundation grant TMSGI2_218095 – FlowState (AT), the Swiss Polar Institute Exploratory Grant 'HI-SLIDE' (AT) and the Natural Environment Research Council 'E4' Doctoral Training Partnership NE/S007407/1 (HP). DEMs provided by the Polar Geospatial Center under NSF-OPP awards 1043681, 1559691, 1542736, 1810976, and 2129685. This study uses Copernicus Sentinel-2 data [2021, 2022] and Sentinel-1 data [2017–2022].

Author contributions

A.T. designed the study, carried out most of the analysis and wrote the manuscript. H.M. processed the SIF measurements, developed the 1-D SIF model, drew Fig. 3 and Suppl. Fig. 1, and contributed to writing the manuscript. H.M., N.C. and N.J. contributed to study design. A.T., H.M., N.C., N.J. and H.P. collected the field measurements. J.D. undertook the hydrological terrain analysis. Dv.A. developed and ran the energy balance model. P.C. and M.T. processed the passive microwave observations of melt extent. S.L. ran the Snow Microwave Radiative Transfer Model and analysed the outputs, and contributed to writing the manuscript. H.M. and A.T. acquired the funding. A.T., H.M., N.C., N.J., H.P., Dv.A., P.C., M.T. and S.L. edited the manuscript.

Competing interests

The authors declare no competing interests.

Additional information

Supplementary information The online version contains supplementary material available at https://doi.org/10.1038/s41467-025-59237-9.

Correspondence and requests for materials should be addressed to Andrew Tedstone.

Peer review information *Nature Communications* thanks the anonymous reviewers for their contribution to the peer review of this work. A peer review file is available.